Characterization of Annular Cement Permeability of a Logged Well Section Using Pressure–Pulse Decay Measurements

Hans Joakim Skadsem

Department of Energy and Petroleum Engineering,
University of Stavanger,
P. O. Box 8600,
Stavanger, Norway;
NORCE Norwegian Research Centre AS,
P. O. Box 8046,
Stavanger, Norway
e-mail: hans.j.skadsem@uis.no

The cement behind casings is an important barrier element in wells that should provide zonal isolation along the well. The hardened cement does not always isolate permeable formations, either due to placement issues or loads that over time compromise the integrity of the barrier. The modern method used to characterize the annular material is ultrasonic logging which provides essential information concerning the type of material behind casing, but no measurement of the annular permeability. This study provides permeability characterization of a casing-cement sandwich joint retrieved from a 33 years old production well that has been logged at surface using a state-of-the-art ultrasonic tool. The joint contains an interval of low-permeable cement that previously has prevented permeability measurement by gas injection. A pressure–pulse decay test method has now been performed that is based on monitoring the evolution of a pressure pulse through the joint. Long-term pressure measurements show communication through the entire joint and are in qualitative agreement with the log. A pressure diffusion model is used to estimate local permeability along the joint, enabling comparison of log response and permeability. The low-permeable region is relatively short, situated directly on top of a casing collar, and has permeability that is orders of magnitude lower than the cement above and below. In the longer term, results from this and related studies can be used as input for future sustained casing pressure evaluations or for quantifying seepage risk behind casings for abandonment designs.
[DOI: 10.1115/1.4053709]

Keywords: deep-water petroleum, petroleum engineering, petroleum wells-drilling/production/construction

1 Introduction

Providing zonal isolation behind casing strings and liners is a critically important function of annular cement. Primary cementing of casings is performed by mixing the cement slurry at surface and normally injecting it down the well inside the casing that is to be cemented, preceded and followed by one or more wiper plugs and fluids, such as washes and spacer fluids [1]. Once in place, the slurry will over time harden into a solid sheath of cement that should act as a low-permeable barrier behind the casing, with recommended permeability less than $200\,\mu$darcy [2]. Some wells however develop sustained casing pressure (SCP) or surface casing vent flows during their productive lifetime, which means that zonal isolation between permeable formations and the surface has not been achieved [3,4]. Incomplete drilling fluid displacement or contamination [5–7], cement shrinkage [8,9], or thermal and mechanical loads during construction or production [10–13] are among the mechanisms that may generate fluid migration paths behind casings and pressure buildup at the surface [14–16].

Once the cement slurry is in place, and it has hardened, the casing shoe and the cement are normally tested through a pressure integrity test or a leak-off test [17,18]. As SCP records and vertical interference tests suggest that realistic microannuli and effective wellbore permeabilities are of the order of tens of micrometer or about 1 darcy or less [19–21], conventional pressure integrity tests cannot be relied upon for detecting such features behind casing. Instead, the main ways of measuring the condition of the material behind casing, and its bonding to the casing, are to use sonic and ultrasonic logging tools [1,22,23]. Such modern tools can identify the material behind casing by combining pulse-echo and flexural wave attenuation [23]. The ultrasonic measurement technique is sensitive to the presence of gas behind casing and detects gas-filled microannuli with micron-sized apertures behind the casing being logged [24]. Other modern developments related to this barrier verification method include the usage of machine learning for improving data processing [25–27]. Learning more about connections between the log response and the conditions of the cement and its permeability can help future decision-making concerning both SCP and well abandonment operations.

The focus of this study is the permeability characterization of a sandwich joint that has been logged both in a well and at the surface using a modern pulse-echo and flexural attenuation tool. The joint is 10 m long and consists of 0.244 m (9 5/8-in.) outer diameter production casing, 0.340 m (13 3/8-in.) outer diameter intermediate casing, and the annular cement sandwiched between the casings. The joint was retrieved as part of the 2018 abandonment operation on a North Sea well which had been in production for more than 30 years at the time of abandonment. The joint, which is referred to as Fish 11, is one of the 26 sandwich joints retrieved from this well as part of this operation. In addition to Fish 11, a second joint referred to as the transition joint was donated by the operator for research purposes. Current research focused on these two sandwich joints is summarized in Refs. [28,29], covering surface re-logging, annular seepage measurements, and cement core analyses.

Previous studies of the two joints have shown that the cemented part of the transition joint contains an effective microannulus of 23–$26\,\mu$m. As will be discussed in more detail later, a complete permeability characterization of Fish 11 has not been performed

previously due to the presence of a low-permeable cement interval that has prevented measurement of steady fluid seepage through the joint. The purpose of this study was therefore to perform a complete permeability assessment of Fish 11 using a pressure–pulse decay method. The relevant low-permeable interval was readily identified on the surface log of the joint and is located directly on top of the casing collar of the inner casing. While conventional permeability measurement of annular cement is normally performed by applying a constant injection pressure and measuring the injection rate of the working fluid, the pressure–pulse decay method is based on monitoring the evolution of a pressure pulse through the joint. A perceived benefit of the pressure–pulse decay method over the conventional method is that it enables permeability measurement in a shorter period of time and is therefore better suited for characterization of low-permeable materials. In much of the existing literature, the test method has been used to effectively measure permeability of tight core material [30–32]. In full-scale and in annular geometries, the method has recently been validated against steady-state seepage results for the more permeable transition joint [33]. Pressure measurements of Fish 11 that are presented in this study will be compared both to the surface acoustic impedance map of Fish 11 and to a pressure diffusion model for the cemented annulus of the joint. By calibrating the model to the pressure measurements, effective local permeability along the annulus is estimated and held up to the cement log. In addition to providing a complete permeability characterization of the sandwich joint, the results may in the longer term also be used as input for future sustained casing pressure evaluations or for quantifying risk of seepage behind casings for well abandonment designs [34,35].

2 The Sandwich Joints and Fish 11

Detailed descriptions of the sandwich joints and some of their main properties are provided in Ref. [28], but pertinent details will be provided below for completeness. The well from which the sandwich joints originated was originally constructed in 1985. The production casing was cemented in two stages due to the existence of a weak zone, with the second stage being reverse circulation cementing of the upper part of the production casing. The sandwich joints were all retrieved from the interval that was reverse cemented. The well developed a history of sustained casing pressure also in the annulus behind the production casing. For the purpose of the recent abandonment operation and for establishing the permanent surface barrier in the well, the upper part of the production casing was first logged using a pulse-echo and flexural attenuation logging tool. The log was subsequently used to determine the upper cut position for retrieval of the production casing above the top-of-cement, followed by cuts through production casing, annular cement, and the intermediate casing, i.e., for retrieval of the sandwich joints. Two of the retrieved sandwich joints are shown in Fig. 1, as received onshore. Fish 11 is shown to the left in this figure.

The Fish 11 was retrieved from a depth between 253.1 m and 263.6 m, and re-logged at surface using the same pulse-echo and flexural attenuation logging tool as was used in the well. The acoustic impedance maps from surface logging at different casing pressures (20, 30, and 40 bar) and under dry and wet conditions are provided in Fig. 2 [28]. Here, dry conditions refer to the joint in its initial condition as received onshore. After completing the dry logging passes, attempts at waterflooding the cemented annular space were performed to saturate the annulus with water and generate what is referred to as wet conditions in Fig. 2. Also shown in the figure are tracks corresponding to azimuthally averaged acoustic impedance measurements under dry and wet conditions. Finally, the right-most track corresponds to the difference between average impedances under wet and dry conditions.

As can be observed from the right-most track in Fig. 2, a marked increase in average acoustic impedance was observed along most of Fish 11 following waterflooding. These regions, at either end of the

Fig. 1 Two cut and pulled sections from a North Sea well. The Fish 11 is shown to the left.

joint, also exhibit significant portions of liquid-like material in the acoustic impedance maps, suggesting hydraulic communication and injectivity. The resulting increase in water-saturation in these parts of the joint compared to the initial "dry" conditions produced the increase in average acoustic impedance observed in the figure. The average acoustic impedance measured over the interval denoted by E in the figure remained largely unchanged, however. The acoustic impedance map suggests mainly solid material in this part of Fish 11. Waterflooding through interval E was not possible between logging passes, suggesting indeed a region of low-permeable cement in this part of Fish 11. Subsequent efforts to inject nitrogen through the joint were limited to the side of Fish 11 above interval E in Fig. 2; it was not possible to measure a steady flowrate of nitrogen through the low-permeable cement in interval E within reasonable experiment duration, and this has so far prevented determination of permeability or effective microannulus size in this part of Fish 11.

Before proceeding, it should be observed that Fish 11 was hung off vertically from the rotary at Ullrigg, the test facility used for both logging and subsequent testing of the sandwich joints, and surface logged upside-down compared to its original orientation in the well [28]. That is, the low-permeable cement interval E in the log was in fact located directly *above* the production casing collar shown in the log. The collar is located at a position of approximately 6.6 m along the tracks in Fig. 2. The significance of this observation will be discussed in more detail below. Furthermore, the fact that the joint was logged vertically implies no readily observed orientation of the wide and narrow sides of the cemented, eccentric annulus in Fig. 2. Below, an attempt will be made to identify the narrow and wide sides based on azimuthal variations in acoustic impedance and the transient pressure measurements.
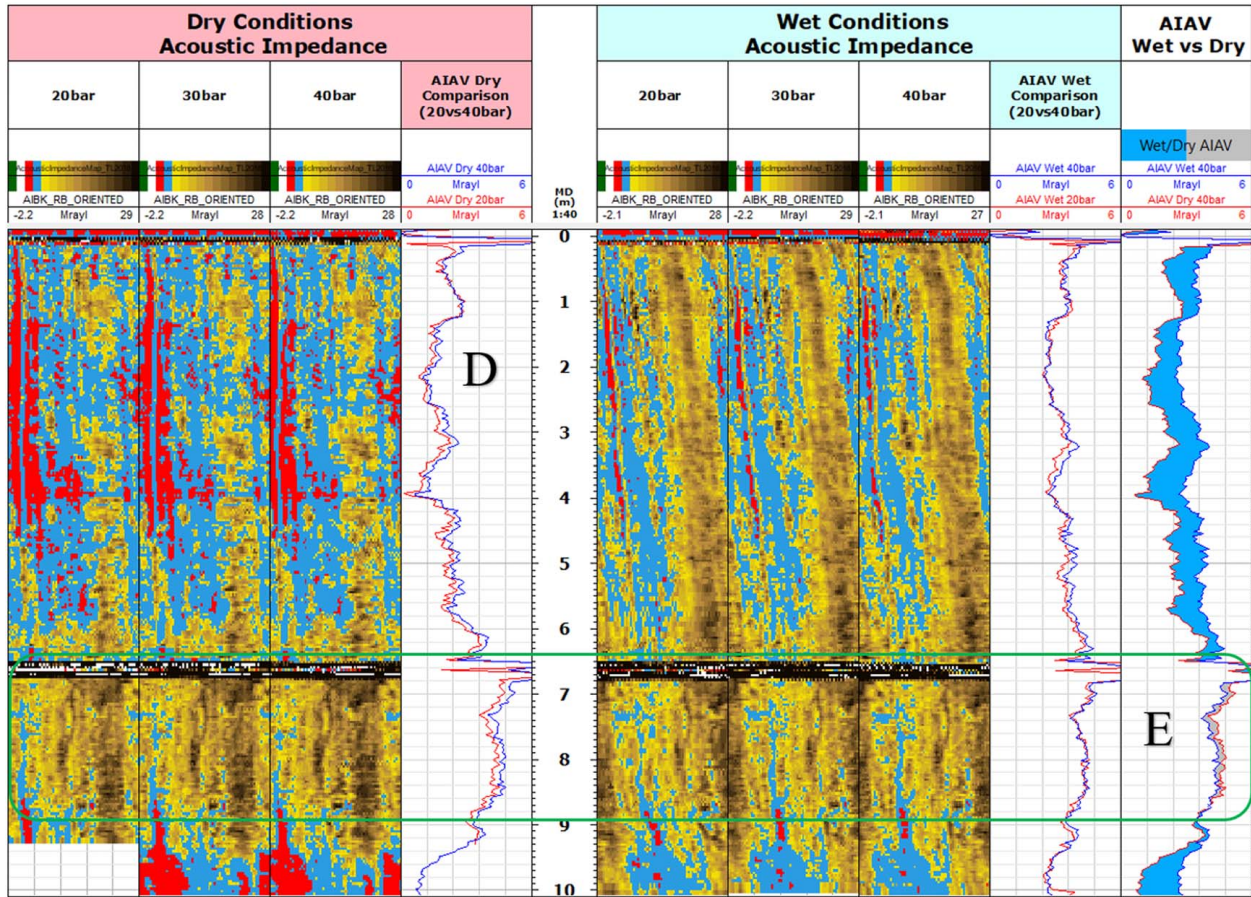
Fig. 2 Acoustic impedance maps from surface re-logging of Fish 11 under dry and under wet conditions and with 20, 30, or 40 bar pressure applied inside the 0.244 m (9 5/8-in.) casing from Ref. [28]. Also shown are tracks showing the azimuthally averaged acoustic impedance at different casing pressures, and the difference in average acoustic impedances under wet and dry conditions. Surface re-logging of the sandwich joint was performed upside-down relative to the original orientation in the well.

Due to low-permeable cement barrier in interval E, all prior permeability characterizations of Fish 11, which have relied on injection of nitrogen at a fixed injection pressure and measuring the resulting flowrate, have been limited to that of the upper half of the log in Fig. 2. In that part of Fish 11, gas seepage corresponding to an effective microannulus of 10.6 μm has been measured [28]. In the current study, experiments utilizing a pressure–pulse decay method will be used to perform a complete permeability characterization of Fish 11, including the low-permeable interval E and the waterflooded interval toward the bottom of Fig. 2.

In preparation of the complete permeability characterization, pressure ports were installed at defined positions along the joint, at the wide side and at the narrow side of the cemented, eccentric annulus. The available test ports in Fish 11 are illustrated in Fig. 3 and compared to the acoustic impedance map at the port positions.

Both ends of the joint were fitted with bulkheads that provide pressure seal for the annulus and the inner casing. The bulkheads were also designed to provide communication to the entire cemented cross section of the annulus at the ends. The bulkhead ports were labeled P1 and P8, with P1 located at the *top* of Fish 11, as seen from its original orientation in the well. This orientation is indicated by the original measured cut depths at P1 and P8 in Fig. 3.

The other ports, labeled from P2 up to P12, were drilled through the cement either on the wide side of the eccentric annulus (even-numbered ports) or on the narrow side of the annulus (odd-numbered ports). These ports were drilled such that they locally penetrate and communicate across the annulus between the two casings. Originally, the first eight ports P1 through P8 were installed
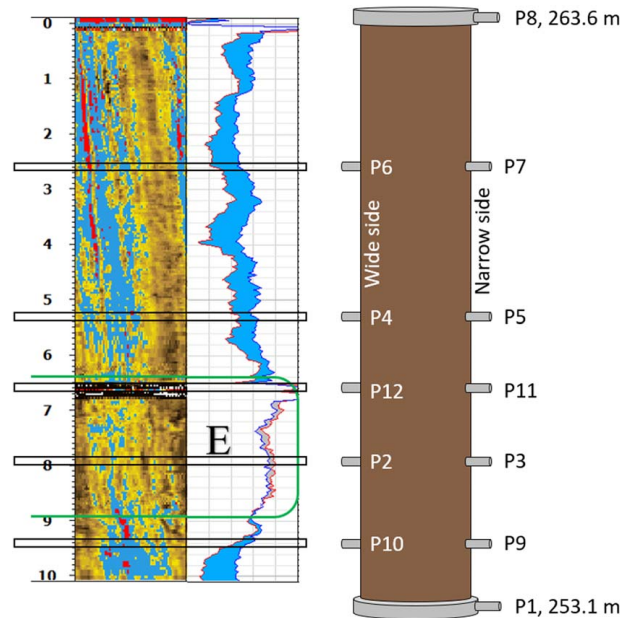

Fig. 3 Illustration of the pressure port locations relative to the 20 bar casing pressure wet acoustic impedance map from Fig. 2. The depths of the end ports P1 and P8 refer to the measured depth of the cut positions in the well. Surface re-logging of the sandwich joint was performed upside-down relative to the original orientation in the well.

Table 1 Configuration of test ports for Fish 11

Test ports	Position measured from P1
P9/P10	1.2 m
P2/P3	2.7 m
P11/P12	4 m (at production casing collar)
P4/P5	5.3 m
P6/P7	8.0 m
P8	10.6 m

in the joint. To improve the spatial coverage particularly in the low-permeable end of the joint, four additional ports P9 through P12 were installed. The exact port positions, measured from P1, are provided in Table 1.

3 Experimental Method and Test Setup

The pressure–pulse decay measurements in Fish 11 reported in this study were performed in Jun. 2021 utilizing the indoor test hall of the Norwegian P&A Laboratories at NORCE in Stavanger, Norway. The tests were performed using the same procedure as in the previous study of the transition joint [33]. The Fish 11 sandwich joint was placed horizontally and insulated to maintain stable body temperature throughout the test program. The measurements were performed by connecting a water-filled upstream reservoir to one side of Fish 11 and a water-filled downstream reservoir of equal volume to the other side. In this study, liquid bottles each of 114 l capacity were used as upstream and downstream reservoirs. The sandwich joint and the two reservoirs are shown in Fig. 4, from the pressure–pulse decay testing of the joint.

Pressure transmitters were mounted at the lines connecting the reservoirs to the test section and at the pressure ports along the length of the test section. A set of valves were used to connect or isolate the fluid reservoirs and the test section. The pressure transmitters used in this study had a working range of 0–250 bar and an accuracy of ±0.02% of the working range. Pressures were logged at a rate of 1 Hz throughout each pressure–pulse decay experiment. In addition to pressure, the temperatures of the two reservoirs and of the exterior body of Fish 11 were monitored throughout.

Before each experiment, both reservoirs and the sandwich joint were brought to the same initial pressure of 20 bar. Once stabilized, a valve between the upstream reservoir and the test section was closed and the upstream reservoir was pressurized to approximately

Fig. 4 Positioning of Fish 11 for permeability characterization using the pressure–pulse decay method. The two bottles at either end of the joint correspond to upstream and downstream reservoirs required for the transient pressure testing.

30 bar, i.e., 10 bar higher than the joint and the downstream reservoir. The test then commenced by instantly opening the same valve and monitoring the propagation of the pressure pulse through the test section and at the downstream reservoir. As the permeability of the sandwich joint varies locally, pressure–pulse decay experiments were performed in both directions to better distinguish these variations. All measurements reported in this paper used water as working fluid. The same test method has previously been validated using the more permeable second sandwich joint and another full-scale annulus test cell in which permeability measurements using the conventional steady-state method were available [33]. The pressure–pulse decay method was considered highly relevant for Fish 11, as the method is perceived to be a more effective approach for particularly low-permeable materials or cement regions. In Fish 11, each test had a duration of approximately 16 h. As will be shown below, a significant pressure difference existed across the low-permeable segment at the end of the test, indicating that complete equilibration would require a vastly longer test period.

4 Pressure Measurements

In the following, pressure measurements along the wide sector (i.e., even-numbered ports) will be presented and compared qualitatively to the acoustic impedance map in Fig. 3. Finally, comparison between wide and narrow sector pressure ports will be shown in order to highlight the few observed differences in hydraulic communication along the opposite sides of the cemented annulus. The presentation begins by considering measurements acquired with the upstream reservoir connected to P1.

4.1 Testing From P1 (253.1 m) to P8 (263.6 m). Pressure measurements along the wide sector of the annulus when testing from P1 are shown in Fig. 5. The plot focuses on the pressure response measured along the wide side of the sandwich joint, i.e., from P1 to P10, P2, P12, P4, P6, and eventually P8, as shown in Fig. 3.

From the measurements, it is apparent that P1 and P10 are well connected as they both reach at the same pressure within the first 25–30 min of the test and remain connected throughout. Following P10, pressure is gradually built at port P2. Based on the comparison between the acoustic impedance map and the port positions, P2 was assumed to be located within a lower permeability region than P10. These measurements support this assumption. An initial pressure response within some 6–7 min was recorded, followed by a very slow pressure buildup to a near-constant level that was some 1.3 bar below that of the upstream P1 and P10. Interestingly, as the pressure measured at P2 started to stabilize after 3–4 h, a gradual pressure increase was recorded at ports downstream of the low-permeable region, i.e., on the collar sensor P12 and at P4, P6, and also P8. The observation that P2 did not stabilize at the same level as P1 and P10 in the test is attributed to the existence of cement with higher permeability downstream of P2, i.e., from P12 and onward to P8.

A detailed view of these downstream pressure measurements is provided in Fig. 6, where the temperature at the downstream reservoir is indicated by yellow curve. The collar sensor P12 responded first to the downstream sensors (orange curve), followed in turn by P4, P6, and P8. Interestingly, we observe relatively good communication between the collar probe and the other downstream sensors in this case. The temperature measurement included in Fig. 6 suggests that the downstream pressure response was indeed due to pressure communication across the low-permeable cement and not due to any systematic temperature variation in the system.

4.2 Testing From P8 (263.6 m) to P1 (253.1 m). Next, Fig. 7 shows the wide side pressure response when the upstream reservoir was connected to port P8, i.e., when reversing the test direction.
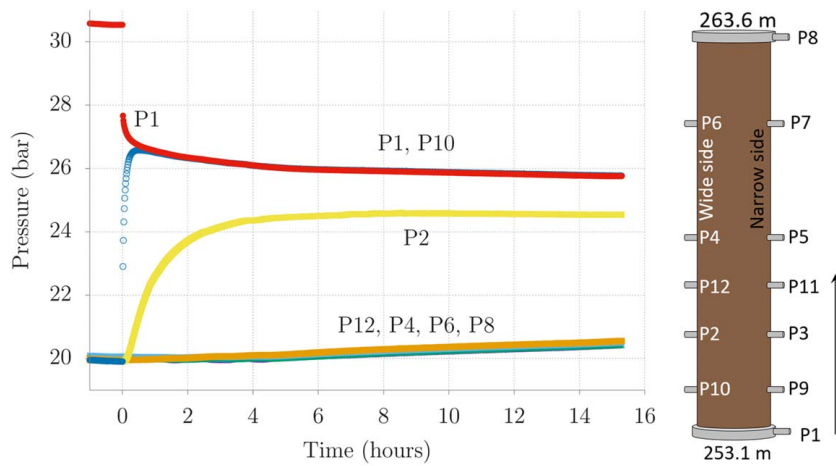
Fig. 5 Pressure–pulse decay measurements in Fish 11 with the upstream reservoir connected to P1 (test direction indicated by the vertical arrow to the right in the figure)
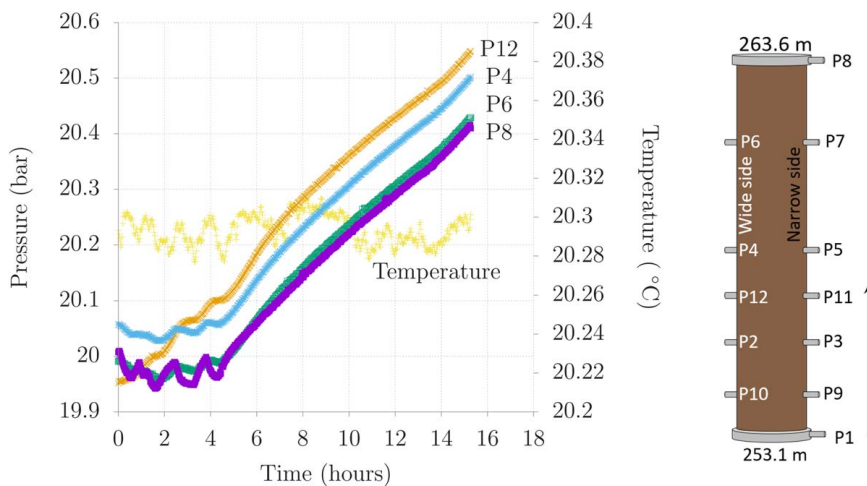

Fig. 6 Detailed view of the downstream pressure measurements in Fig. 5. The upstream reservoir was connected to port P1 (test direction indicated by the vertical arrow to the right in the figure). Also shown in the figure to the left is the measured temperature at the downstream reservoir, connected to P8.
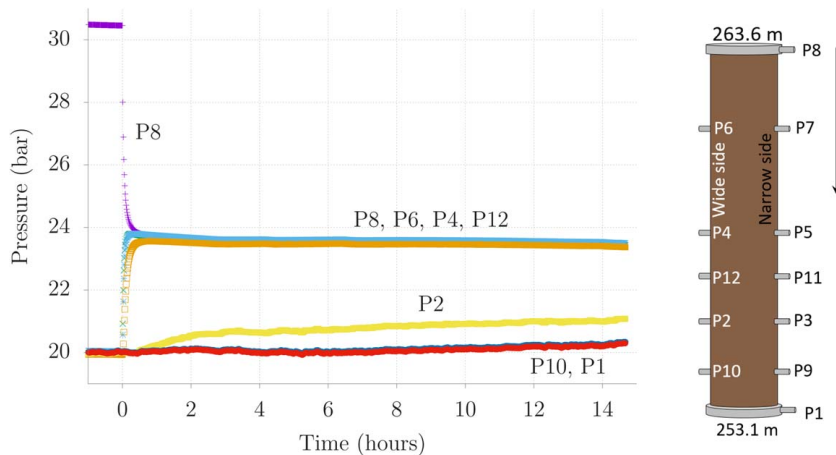

Fig. 7 Pressure–pulse decay measurements in Fish 11 with the upstream reservoir connected to P8 (test direction indicated by the vertical arrow to the right in the figure)
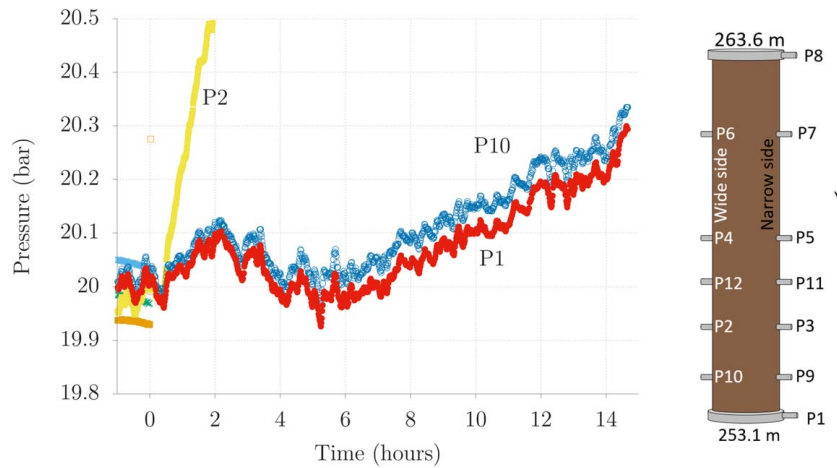
Fig. 8 Detailed view of the downstream pressure measurements in Fig. 7. The upstream reservoir was connected to P8 (test direction indicated by the vertical arrow to the right in the figure).

The measurements indicate again relatively quick pressure communication along the wide side of the annulus, from P8 to P6, P4, and to P12, the latter of which corresponds to the orange curve. This observation agrees well with that in Fig. 6, i.e., these locations are well connected and there is quick pressure communication in this part of the joint. Similar to Fig. 5, a very gradual pressure buildup was observed at port P2, assumed to be in the low-permeable cement region. After approximately 25–30 min since the start of the test, the first response was observed on P2. The pressure responses at the far downstream locations were significantly slower, as shown in the detailed view in Fig. 8. As before, the turquoise and red curves correspond to P10 and P1, respectively. The measurements in Fig. 8 indicate good pressure communication between these far downstream ports, in agreement with the observation in Fig. 7. Finally, the measurements shown in the detailed view in Fig. 8 appear less smooth than when testing from P1, i.e., Fig. 6. This was due to temperature compensation of the downstream pressure measurements when testing from P8; the temperature of the downstream reservoir at P1 increased by more than 0.1 °C over the course of the test, and this temperature increase corresponded to a pressure increase of approximately 0.4 bar in the downstream reservoir. As this is comparable in magnitude to the pressure increase due to pressure communication across the collar segment, the measurements in Fig. 8 have been compensated for the temperature variation and should as such represent the actual pressure transmission across the low-permeable zone. No such compensation was done on the pressure measurements in Fig. 6 as the downstream reservoir was maintained at a practically constant temperature throughout that test.

4.3 Comparison of Wide and Narrow Sides of the Cemented Annulus. From the acoustic impedance map in Fig. 3, one can observe clear azimuthal variations in material type along most of the sandwich joint. In the region of Fish 11 between P8 (263.6 m) and the collar (P11 and P12), a connected region of liquid material behind the production casing was identified. As the joint was logged vertically and unoriented, it is not clear from the map itself whether the liquid material primarily occupies the wide or the narrow side of the annulus. Liquid was also identified at the opposite end of the section between P1 (253.1 m) and P9/P10.

In Fig. 9, comparisons of wide side (even-numbered) and narrow side (odd-numbered) pressure measurements are provided. As indicated by the title of each panel, they correspond to alternatively testing from P1 and from P8, and focus on the pressure measurements in the low-permeable region (P2 and P3) and between P1 (253.1 m) and adjacent to this low-permeable region (P9 and P10).

Pressure measurements acquired when testing from P1 are shown in the left and center panel in the figure. Considering first the pressure measurements at P9 and P10, in the left-most figure, a distinct asymmetry between wide and narrow sides can be seen. While pressure communication between the upstream reservoir at P1 and the adjacent wide side port P10 was gradual and occurred over some 30 min, communication between the reservoir and the narrow side port P9 was practically immediate. This observation suggests that the liquid (blue) material at ports P9 and P10 in the acoustic impedance map in Fig. 3 is indeed located at the *narrow* side of the annulus, i.e., port P9 is connected to this liquid region in the acoustic impedance map.

Moving on to the center panel in Fig. 9 and the pressures measured within the low-permeable region, there was now less difference between wide and narrow side measurements. The pressure response was slightly faster along the narrow side (P3). When reversing the test direction and connecting port P8 to the upstream reservoir, the right-most panel in the figure indicates again a minor asymmetry between wide and narrow sides, suggesting a difference in local permeability. Also in this case, pressure transmission along the narrow side of the annulus progressed faster than along the wide side. The remaining pressure measurements are *not* included in these figures as they showed practically *no* difference in pressure response between wide and narrow sides. That is, measurements at the collar (P11 and P12) and between the collar and P8 gave no discernible difference in pressure responses at the wide and narrow sides while testing from either direction. This indicates azimuthal pressure communication in this part of Fish 11, which again is in agreement with the acoustic impedance map which identifies significant and connected regions of liquid material in the joint from the collar to P8.

To conclude the qualitative comparison between the acoustic impedance map and the pressure measurements, we note the following main observations:

- Relatively quick pressure communication was observed along Fish 11 from P8 through P6/P7, P4/P5, and to the collar and ports P11/P12. The ports along the wide side (even-numbered) were in all cases hydraulically well connected to ports along the narrow side (odd-numbered). These observations agree qualitatively with the identification of significant connected regions of liquid material behind the production casing in this part of the joint.
- Similar connectivity was observed at the other end of Fish 11, from P1 through P9/P10. Studying the initial pressure transient when testing with the upstream reservoir connected to P1, it was found that the narrow side P9 was significantly better
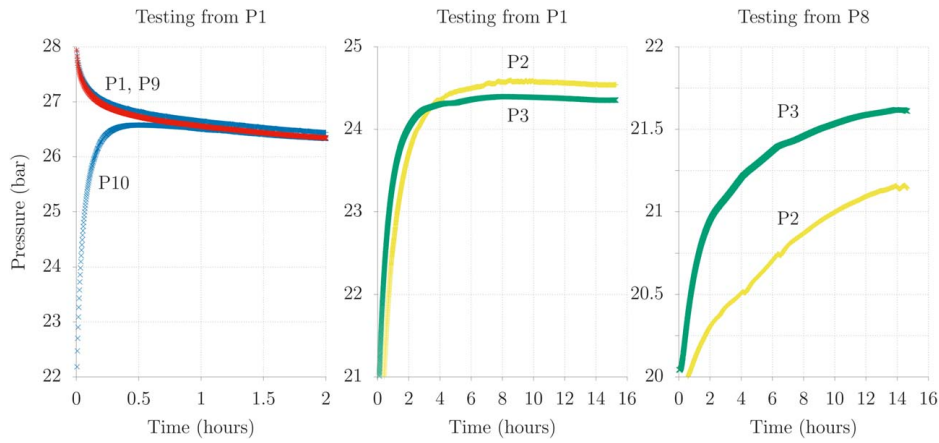
Fig. 9 Detailed views of measurements of pressure that were different along the wide and narrow sides of the annulus in Fish 11

connected to P1 than the wide side P10 port was. The pressure measurements suggest near full and unrestricted communication between P9 and P1. These observations are also in agreement with the acoustic impedance map, considering the identification of a significant liquid material region between P9/P10 and P1 that covers approximately half of the circumference of the inner casing. Furthermore, the asymmetric pressure response suggests that the narrow side pressure port, P9, is within the liquid material region in the acoustic impedance log in Fig. 3, suggesting that the middle portion of the map corresponds to the narrow side of the annulus.

- The transient pressure measurements clearly indicated the existence of a low-permeable region separating regions with relatively quick pressure communication at either end of the joint. Measurements at P2 and P3 ports which are both within the region of low-permeable cement showed some asymmetry between wide and narrow sides, with the narrow side producing the slightly quicker response. The acoustic impedance map identified narrow channels of liquid-like material in this interval, and their position is consistent with the assumption of the narrow side of the annulus being along the middle portion of the map.

The above comparisons between transient pressure measurements and the acoustic impedance map give highly consistent qualitative results concerning the rate of pressure communication at either side of the low-permeable interval and of communication across the eccentric annulus. In the next section, a pressure diffusion model will be introduced that connects the measured transient pressure evolution in Fish 11 to the local annulus permeability. By calibrating the model to the pressure measurements, permeabilities can be assigned to the different annular regions in Fish 11.

5 Pressure–Pulse Decay Model for Fish 11

As the full-scale transient pressure tests were performed similar to how pressure–pulse decay experiments are more traditionally performed on cores [30–32], a physical model for the pressure propagation through Fish 11 can be developed within this established framework. In the following, the pressure evolution model used in our previous study will be further generalized to three main regions of different permeabilities [33]. Consider now the model geometry shown in Fig. 10, where the test direction is assumed to be from P1 to P8 with the upstream reservoir connected to P1.

The three regions are defined by their local, effective permeability k_i with k_1 being the permeability of the region adjacent to port P1, and the locations of the interfaces, ℓ_{12} and ℓ_{23}, measured from P1. These characteristics of Fish 11 were not established at the time of the experiments and will be determined below by calibrating the pressure diffusion model presented in this section to the transient measurements.

Within each of the three regions, it is assumed that the pressure p evolves according to the one-dimensional diffusion equation

$$\frac{dp}{dt} = \frac{k_i}{\mu c} \frac{d^2 p}{dx^2} \tag{1}$$

where t is time and x is the axial position, measured from the upstream reservoir. When using the one-dimensional diffusion equation, it is assumed that the pressure at a given axial position along the test section is the same around the circumference of the annulus. It is also assumed, for simplicity, that the annulus can be considered as a single permeability medium. Further, k_i ($i = 1, 2, 3$) denotes the local permeability, μ is the viscosity of the working fluid, and c denotes the compressibility of the region, which is given by the combined compressibility of the working
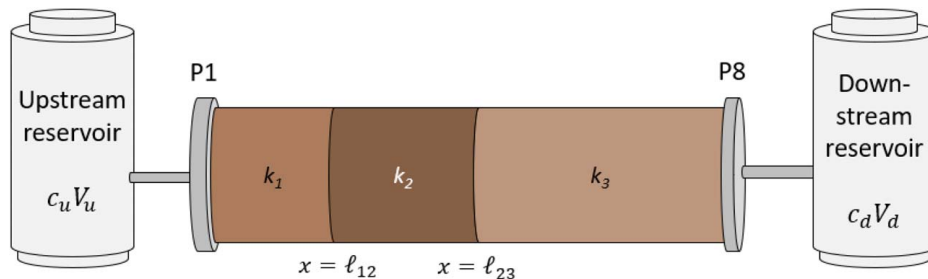

Fig. 10 Illustration of the geometry used for defining a pressure diffusion model to represent the pressure–pulse decay measurements in Fish 11. The reservoirs are oriented as they would for a test from P1 to P8.

fluid and the elastic compliance of the casing and annular cement.

At an interface $x = \ell$ between adjacent regions, the pressure and the flux are required to be continuous [36]:

$$\lim_{x \to \ell^-} p = \lim_{x \to \ell^+} p, \qquad k_i \frac{dp}{dx}\bigg|_{x \to \ell^-} = k_{i+1} \frac{dp}{dx}\bigg|_{x \to \ell^+} \qquad (2)$$

Finally, at the upstream and downstream reservoirs, the following boundary conditions apply:

$$c_{res,u} V_u \frac{dp_u}{dt} = \frac{k_1 A}{\mu} \frac{dp}{dx}\bigg|_{x \to 0}, \qquad c_{res,d} V_d \frac{dp_d}{dt} = -\frac{k_3 A}{\mu} \frac{dp}{dx}\bigg|_{x \to L} \qquad (3)$$

where the test direction is as per Fig. 10, $c_{res,u}$ and V_u denote the compressibility and volume of the upstream reservoir, respectively, and p_u is the pressure of the upstream reservoir. The same quantities $c_{res,d}$, V_d, and p_d are also defined for the downstream reservoir. Finally, A denotes the annular cross-sectional area of Fish 11. As initial condition, the pressure throughout Fish 11 is set equal to the downstream reservoir, i.e., $p(x, t=0) = p_d$, and the upstream reservoir is set equal to the higher pressure initial pressure used in the tests, $p_u(t=0) > p_d(t=0)$. A similar pressure diffusion model with a single, internal permeability interface was presented in Ref. [33]. As that joint contained the top-of-cement along the middle of the joint, this acted as a natural permeability interface in the transition joint. Its location, and the permeability of the regions on either side, were determined by calibrating the model to measurements made in the transition joint.

The pressure diffusion model defined above is solved by Laplace transforming the diffusion equation (1) in each interval. The integration constants are fixed through the boundary conditions in Eqs. (2) and (3). Finally, the complete solution is numerically inverted to the time-domain using the Stehfest algorithm [37].

To close the above equations, measurements are required of the effective compressibility of Fish 11, c, and of the two reservoirs, $c_{res,u}$ and $c_{res,d}$. These were measured by pressurizing each of these vessels individually to an initial pressure of 20 bar (for Fish 11) or 30 bar (for the two reservoirs) and then bleeding the pressure down in steps while collecting the effluent. At the relevant test pressures, plotting the vessel pressure as a function of drained volume yields a linear curve with negative slope. The magnitude of the slope is taken as $(cV)^{-1}$ or the inverse of the compressive storage of the vessel, cV, where V is the vessel volume. The compressive storage defines the required volume to be injected or produced to change the vessel pressure by a unit pressure.

Measurements of vessel pressure for both Fish 11 and the two reservoirs as a function of the drained fluid volume are provided in Fig. 11.
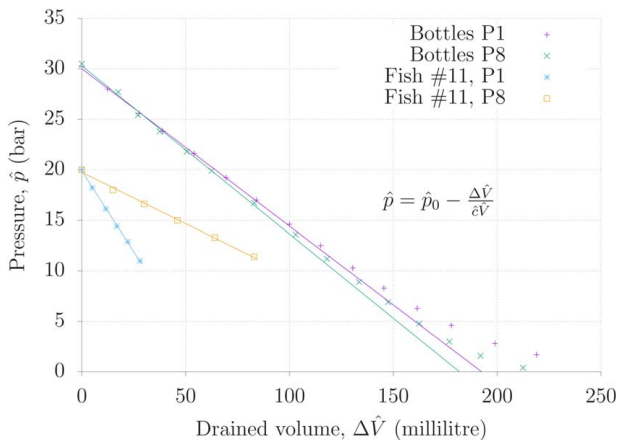

Fig. 11 Measurements of vessel pressure as a function of drained volume for determination of the compressive storage of the reservoirs and Fish 11

The reservoirs are labeled "Bottles P1" and "Bottles P8." As the relevant working pressures for the tests discussed above are between 20 and 30 bar, measurements from this range were used to produce a linear fit to the equation shown in the figure. For the reservoirs, a compressive storage of $c_{res,u} V_u \approx c_{res,d} V_d = 6.21 \cdot 10^{-11}$ m^3/Pa is found. For Fish 11, the end ports P1 and then P8 were used for compressive storage estimation. Since the low-permeable cement region effectively isolates the far side of the joint and since the annular volumes are different on either side of the low-permeable cement, two different slopes are found in Fig. 11. Normalizing the measurements to the entire annular volume of Fish 11, a compressive storage of $cV = 1.6 \cdot 10^{-10}$ m^3/Pa is found. The corresponding value for the Transition joint was found to be $cV = 2.1 \cdot 10^{-10}$ m^3/Pa [33].

5.1 Comparison Between Model Results and Experiments.
It now remains to determine the locations ℓ_{12} and ℓ_{23} and the effective permeability of each region. Based on the evidence in the acoustic impedance map, it will be assumed that ℓ_{23} is at the collar of the production casing, i.e., coinciding with ports P11 and P12 in Fig. 3. From the assessment above, it is further anticipated that the second interface, $x = \ell_{12}$, is located between P1 and ports P2/P3. A more precise determination of this interface position and the associated permeability of each region will be made by comparing the model results to measured data below. While it is apparent from Fig. 9 that the effective permeability may be different along the wide and narrow sides of the annulus, a single, effective value will be used for each region in the model of Fish 11.

Following an iterative process that consists of adjusting the second interface position and the permeability values, satisfactory agreement between model predictions and measurements has been achieved when testing both from P1 and from P8. In what follows, model predictions based on the following assumptions will be shown and compared to the experimental measurements:

- Interface positions are located at $\ell_{12} = 2.35$ m and $\ell_{23} = 4$ m, measured from port P1
- Permeability in $0 < x < \ell_{12}$: $k_1 = 6.7$ mdarcy (13.5 μm equivalent microannulus)
- Permeability in $\ell_{12} < x < \ell_{23}$: $k_2 = 16.7 \, \mu$mdarcy (1.8 μm equivalent microannulus)
- Permeability in $\ell_{23} < x < L$: $k_3 = 10.0$ mdarcy (15.4 μm equivalent microannulus)

The conversion between permeability k_i and effective microannulus above is based on the assumption that the effective microannulus is located adjacent to the inner wall of the outer casing, and the equivalence between the Darcy equation and the Hagen–Poiseuille result for flow between flat plates, i.e., $kA \leftrightarrow Wh^3/12$, with W the circumference of the inner wall of the outer casing and h the microannulus gap width [21].

Shown in Fig. 12 are the pressure measurements (points) along the wide side of the annulus when testing from P1 and the numerical model predictions (lines) using the permeability interface positions specified above. A detailed view of the downstream sensor measurements and model prediction is provided in Fig. 13.

The two figures indicate that the model captures the main features observed in the experiments, including the rapid pressure communication between P1 and P10, the partial pressure buildup in the low-permeable region (P2), and the gradual, connected pressurization downstream of the low-permeable region. We note a small, initial pressure offset among the measurements shown in Fig. 13 that is not present in the model results where the initial pressure is set to 20 bar everywhere except in the upstream reservoir. In spite of this initial difference between measurements and model predictions, we observe an excellent correspondence between the measured and predicted pressure buildup rates at later times in the test.

Ideally, the same model should be capable of describing the reverse pressure–pulse decay tests, i.e., when the upstream reservoir was connected to port P8. In Fig. 14, comparison is provided
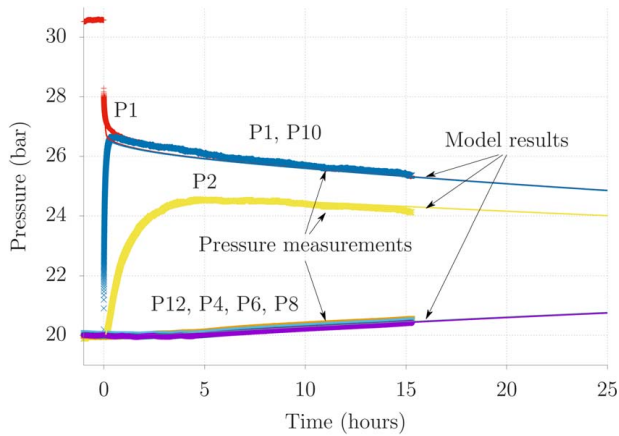
Fig. 12 Comparison of pressure–pulse decay measurements with the upstream reservoir at P1 to predictions of the calibrated pressure diffusion model

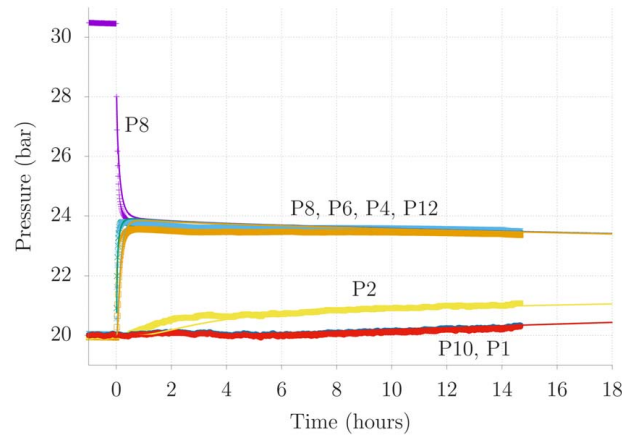**Fig. 14 Comparison of pressure–pulse decay measurements with the upstream reservoir at P8 to predictions of the calibrated pressure diffusion model**
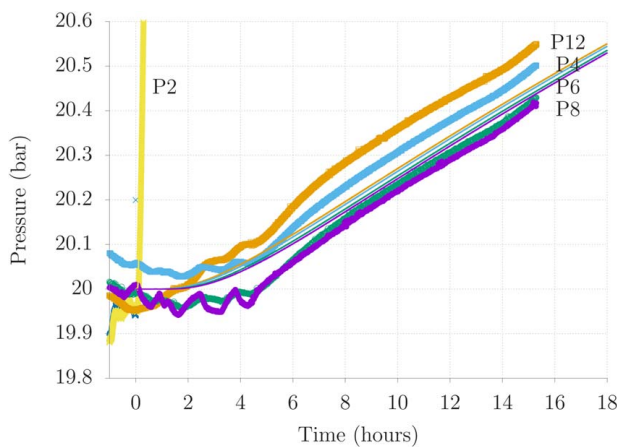
temperature compensation has not completely eliminated this effect, and this could explain the numerical offset between measured and predicted pressures.

To quantify the deviations between pressure measurements and model predictions, the root-mean-square deviation (RMSD) has been evaluated for each pressure port as

$$\mathrm{RMSD} = \sqrt{\sum_{i=1}^{N} (\hat{p}_i - p_i)^2 / N}$$

where $\hat{p}_i$ denotes pressure measurement at time $t = t_i$, p_i is the corresponding model prediction at the same pressure port and at the same time, and N denotes the total number of pressure measurements in the time-series. The RMSD values have been evaluated for pressure measurements at each port and for either test direction and are summarized in Table 2.

The largest deviations are associated with the offsets between measurements and model predictions at ports P4 and P12 when testing from P8, as seen in the left graph of Fig. 15. In spite of the small offset between model and measurements, the calibrated model is considered to satisfactorily represent the actual behavior of Fish 11 when testing from either side.

Fig. 13 Detailed view of the downstream pressure measurements and model predictions from Fig. 12

6 Discussion

A summary of the main output from the transient pressure modeling is provided in Fig. 16, where the three regions, their position, and permeability are indicated and compared to the acoustic impedance map. Also indicated along the acoustic impedance map is the likely orientation of the narrow side of the eccentric annulus based on the qualitative assessment of the pressure measurements discussed above. This assumed orientation is largely based on the pressure responses when testing from P1 but is also supported by the

between measurements (points, up to nearly 15 h) and model predictions (lines, drawn to approximately 24 h). While some variation is seen in the pressure measurement and model prediction within the low-permeable region (yellow points and curve, P2), the overall pressure response is well represented by the calibrated model introduced above.

More detailed views of the early-time evolution of the pressures measured adjacent to the upstream reservoir and the late-time evolution of the downstream pressures are provided in Fig. 13. Beginning with the early-time pressure responses to the left in the figure, it can be observed that the measurements appear to stabilize at a slightly lower value than the model predictions, but that the time until stabilization is approximately the same in both experiments and in the model results. The slight difference between measured and modeled pressure levels in the left figure is attributed to uncertainty in the compressive storage assessment of this side of Fish 11.

Moving on to the downstream pressure measurements at the far side of the low-permeable cement, i.e., P10 and P1 (blue and red points) in the right graph in Fig. 13, it can be observed that the model predicts accurately the pressure buildup rate from approximately 6 hours into the test. As pointed out above and seen by the less smooth pressure measurements in the figure, temperature compensation of the pressure measurements were necessary to eliminate approximately 0.4 bar of temperature-induced pressure-drift in the downstream reservoir connected to P1. The initial pressure response within the first 4 h at both P1 and P10 suggests that

Table 2 Root-mean-square deviations for the time-series measurements and model predictions

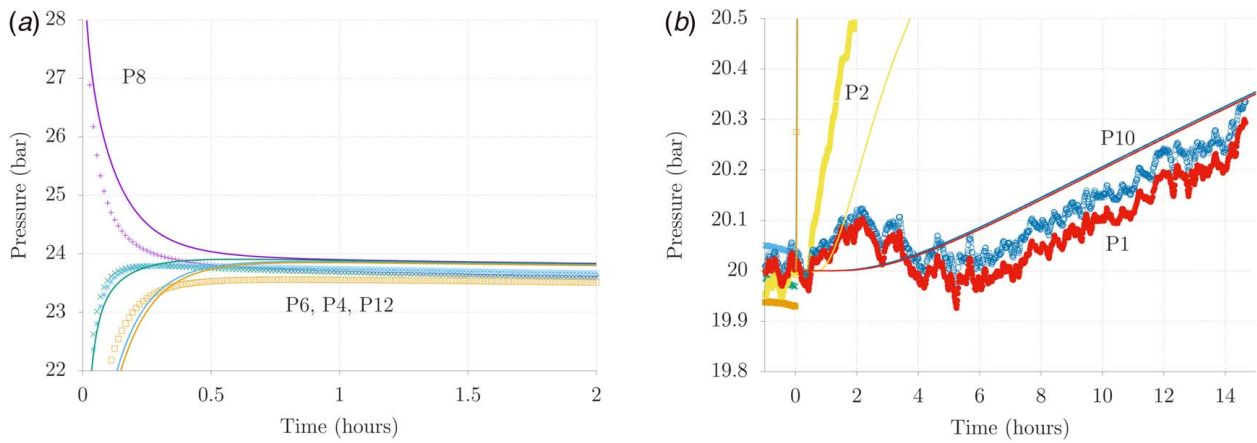| Test port	Testing from P1 (bar)	Testing from P8 (bar)
P1	0.17	0.09
P2	0.13	0.13
P4	0.04	0.22
P6	0.03	0.14
P8	0.04	0.17
P10	0.17	0.06
P12	0.07	0.21

Fig. 15 (a) Detailed view of pressure measurements and model predictions adjacent to the upstream reservoir and (b) downstream the low-permeable interval. The upstream reservoir is connected to port P8.
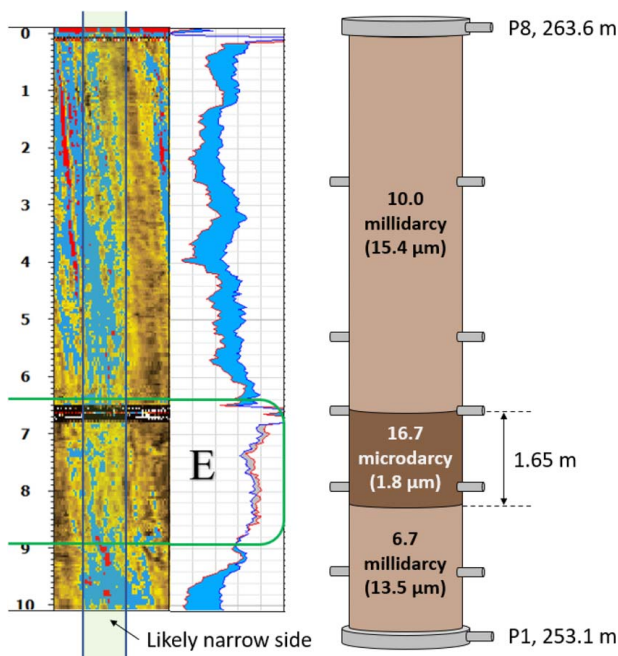

Fig. 16 Comparison of the acoustic impedance map of Fish 11 and the calibrated pressure diffusion model

observation in Fig. 15 that wide side ports P4 and P6 appear connected. The orientation indicated in the figure assumes that the tool itself did not rotate as it was pulled up along the joint.

As remarked above, the effective microannulus of the cemented annulus between P8 and ports P4/P5 was previously measured to be 10.6 μm. The measurement was made by applying up to 5 bar nitrogen pressure at port P8 and keeping either P4 or P5 open to atmosphere and recording the injection rate at P8 [28]. As shown in Fig. 16, an effective microannulus of 15.4 μm is found in this part of the joint based on the transient pressure–pulse decay experiments and the subsequent model calibration. The slightly higher result found from the pressure–pulse decay experiments can be attributed to the higher test pressures applied as part of the transient tests, which can affect the permeability by elastic deformation of the casings and annular cement. However, when considering that the two methods of measuring the permeability or effective microannulus are entirely independent, and that the measurements were performed more than 12 months apart, the agreement between the two is considered satisfactory and the measurements consistent.

The permeability or effective microannulus of the annular cement next to P1 and at the collar have not been possible to measure previously by gas injection. The transient pressure–pulse decay measurements presented above clearly demonstrate pressure communication through the interval with low-permeable cement. When testing either from below the collar, as originally oriented in the well (i.e., from P8), or from above, a clear pressure response on the far side of the low-permeable interval was found after some 6–8 h. The calibrated numerical model recreated the qualitative features observed in both experiments and gave satisfactory quantitative agreement to transient pressure measurements.

By qualitatively inspecting the original pulse-echo and flexural attenuation log from the well, shown in Ref. [28], one can identify additional relatively short intervals with cement bond quality similar to that of the low-permeable interval in Fish 11. A common feature among these intervals is that they tended to be above the casing collars of the production casing. This part of the well is nearly vertical and was cemented by bullheading a neat Class-G cement slurry down the annulus. Being apparently connected to the geometric feature of the collar, the locally improved cement bond is thought to be associated with vertical sedimentation of cement particles on top of the collar after the cement slurry was pumped in place and/or by improved fluid displacement due to narrower annular cross section at the collar. While remaining inconclusive, a current hypothesis is that the lack of anti-settling additives in the neat slurry resulted in sedimentation of individual cement particles or settling of flocs of particles on top of the collars [1]. An increased concentration of cement particles on top of the collar would result in a higher cement density and, at least in the case considered here, a better cement bond to casing and lower permeability compared to annular cement below or further above the casing collar. In their review of the inter-particle potential and application of the electric double-layer model to neat cement slurries, Yang et al. [38] found that normal, neat cement slurries tend to be coagulated suspensions. That is, the inter-particle potential is considered to be attractive and without a secondary minimum that could result in a flocculated suspension. In a coagulated suspension, particles rapidly and irreversibly approach the primary minimum of the potential function, resulting in vertical settling of flocs containing particles of different size [38]. In their study of sedimentation and settling in cement slurries, Stiles and Baret [39] compared experimental measurements to models for free sedimentation in a stable dispersion and for settling of flocs of cement particles. Their study found that the model based on settling of flocs correlated better to experimental measurements than the free sedimentation model, consistent with the subsequent analysis of Yang et al. [38]. Further studies are required to finally conclude on the precise mechanism that gave rise to the low-permeable cement intervals at the collars of the production casing in this well.

Finally, it should be pointed out that modeling the sandwich joint Fish 11 as done above, i.e., by three regions of different effective permeability is necessarily a simplification and only an approximation of the actual, local permeability variations along the joint. The discretization of Fish 11 shown in Fig. 16 has in this study been found to provide a relatively good representation of transient pressure evolution at both short time-scales (close to the upstream reservoirs) and also longer time-scales (several hours, downstream). While the actual conditions of the cement in the annular space remain unknown, the pressure–pulse decay measurements presented in this study have provided new and improved insights into correlations between ultrasonic logs, here represented by the acoustic impedance map and the effective annular permeability.

7 Summary and Conclusion

This study has focused on the acoustic impedance map and the permeability characterization of Fish 11, a sandwich joint retrieved from a 33 years old production well. Where previous attempts at measuring the annular permeability of the cement were limited to the more permeable segment of the joint, the current study utilizes a pressure–pulse decay method for complete permeability evaluation. The test method relies on monitoring the evolution of a pressure pulse through the joint and is equivalent to transient pressure testing of low-permeable core material. Excellent qualitative agreement is observed between pressure measurements and the acoustic impedance map of the joint, and the quantitative analysis of the pressure measurements yields local permeability values for the annular cement. A clear correspondence is found between the region of lowest permeability and highest acoustic impedance.

Previous experiments using the pressure–pulse decay method for permeability characterization have shown good quantitative agreement with available steady-state seepage data. Also in the current study, we find agreement between the two test methods where it was possible to perform steady-state measurements. The main advantage of the transient measurement protocol is that it enables characterization of low-permeable regions where it otherwise is very time-consuming or difficult to establish steady seepage. The main results of this study are summarized visually in Fig. 16, where the detailed acoustic impedance map is connected to the permeability measurements. As the current prevalent method for measuring the condition of the material behind casing is sonic and ultrasonic logging tools, this information can serve as input for linking log responses and seepage potentials. The results can potentially also be valuable for future sustained casing pressure evaluations or for quantifying risk of seepage behind casings for well abandonment designs [34,35].

Conflict of Interest

There are no conflicts of interest.

Data Availability Statement

The data and information that support the findings of this article are freely available. The author attest that all data for this study are included in the paper. Data provided by a third party are listed in Acknowledgment.

Nomenclature

c = compressibility, $M^{-1}LT^2$, 1/Pa
h = microannulus gap width, L, m
k = permeability, L^2, darcy,
p = pressure, $ML^{-1}T^{-2}$, Pa
t = time, T, s
x = axial coordinate, L, m
A = cross section, L^2, m^2
L = axial length of sandwich joint, L, m
V = volume, L^3, m^3
W = circumference, L, m
μ = viscosity, $ML^{-1}T^{-1}$, Pa·s

References

[1] Nelson, E. B., and Guillot, D., eds., 2006, *Well Cementing*, 2nd ed., Schlumberger, Sugar Land, TX.

[2] Wu, Y., Patel, H., Salehi, S., and Mokhtari, M., 2020, "Experimental and Finite Element Modelling Evaluation of Cement Integrity Under Diametric Compression," J. Petrol. Sci. Eng., **188**, p. 106844.

[3] Bourgoyne, A. T., Scott, S. L., and Regg, J. B., 1999, "Sustained Casing Pressure in Offshore Producing Wells," Offshore Technology Conference (OTC) 11029, Houston, TX, May 3–6, pp. 1–13.

[4] Davies, R. J., Almond, S., Ward, R. S., Jackson, R. B., Adams, C., Worrall, F., Herringshaw, L. G., Gluyas, J. G., and Whitehead, M. A., 2014, "Oil and Gas Wells and Their Integrity: Implications for Shale and Unconventional Resource Exploitation," Marine Petrol. Geol., **56**, pp. 239–254.

[5] McLean, R. H., Manry, C. W., and Whitaker, W. W., 1967, "Displacement Mechanics in Primary Cementing," J. Pet. Technol., **19**(2), pp. 251–260.

[6] Bittleston, S., and Guillot, D., 1991, "Mud Removal: Research Improves Traditional Cementing Guidelines," Oilfield Rev. (Netherlands), **3**(2), pp. 44–54.

[7] Agbasimalo, N., and Radonjic, M., 2014, "Experimental Study of the Impact of Drilling Fluid Contamination on the Integrity of Cement-Formation Interface," ASME J. Energy Resour. Technol., **136**(4), p. 042908.

[8] Parcevaux, P. A., and Sault, P. H., 1984, "Cement Shrinkage and Elasticity: A New Approach for a Good Zonal Isolation," SPE Annual Technical Conference and Exhibition, Houston, TX, pp. 1–12, SPE-13176-MS.

[9] Sabins, F. L., and Sutton, D. L., 1991, "Interrelationship Between Critical Cement Properties and Volume Changes During Cement Setting," SPE Drill. Eng., **6**(2), pp. 88–94.

[10] Goodwin, K. J., and Crook, R. J., 1992, "Cement Sheath Stress Failure," SPE Drill. Eng., **7**(4), pp. 291–296 (SPE-20453-PA).

[11] Jackson, P., and Murphey, C., 1993, "Effect of Casing Pressure on Gas Flow Through a Sheath of Set Cement," SPE/IADC Drilling Conference and Exhibition, Amsterdam, The Netherlands, Feb. 23–25, pp. 1–10.

[12] Bois, A.-P., Garnier, A., Rodot, F., Saint-Marc, J., and Aimard, N., 2011, "How to Prevent Loss of Zonal Isolation Through a Comprehensive Analysis of Microannulus Formation," SPE Drill. Complet., **26**(1), pp. 13–31.

[13] Patel, H., and Salehi, S., 2019, "Development of an Advanced Finite Element Model and Parametric Study to Evaluate Cement Sheath Barrier," ASME J. Energy Resour. Technol., **141**(9), p. 092902.

[14] Xu, R., and Wojtanowicz, A., 2001, "Diagnosis of Sustained Casing Pressure From Bleed-Off/Buildup Testing Patterns," SPE Oklahoma City Oil and Gas Symposium/Production and Operations Symposium, pp. 1–15, SPE-67194-MS.

[15] Rocha-Valadez, T., Hasan, A., Mannan, S., and Kabir, C., 2014, "Assessing Wellbore Integrity in Sustained-Casing-Pressure Annulus," SPE Drill. Complet., **29**(1), pp. 131–138.

[16] Santos, L., and Dahi Taleghani, A., 2021, "On Quantitative Assessment of Effective Cement Bonding to Guarantee Wellbore Integrity," ASME J. Energy Resour. Technol., **144**(1), p. 013001.

[17] Postler, D., 1997, "Pressure Integrity Test Interpretation," SPE/IADC Drilling Conference and Exhibition, SPE-37589-MS.

[18] Altun, G., Shirman, E., Langlinais, J. P., and Bourgoyne, A. T. J., 1999, "New Model to Analyze Nonlinear Leak-Off Test Behavior," ASME J. Energy Resour. Technol., **121**(2), pp. 102–109.

[19] Gasda, S. E., Celia, M. A., Wang, J. Z., and Duguid, A., 2013, "Wellbore Permeability Estimates From Vertical Interference Testing of Existing Wells," Energy Proc., **37**(1), pp. 5673–5680.

[20] Kang, M., Baik, E., Miller, A. R., Bandilla, K. W., and Celia, M. A., 2015, "Effective Permeabilities of Abandoned Oil and Gas Wells: Analysis of Data From Pennsylvania," Environ. Sci. Technol., **49**(7), pp. 4757–4764.

[21] Stormont, J. C., Garcia Fernandez, S., Taha, M. R., and Matteo, E. N., 2018, "Gas Flow Through Cement-Casing Microannuli Under Varying Stress Conditions," Geomech. Energy Environ., **13**(4), pp. 1–13.

[22] van Kujik, R., Zeroug, S., Froelich, B., Allouche, M., Bose, S., Miller, D., Le Calvez, J.-L., Schoepf, V., and Pagning, A., 2005, "A Novel Ultrasonic Cased-Hole Imager for Enhanced Cement Evaluation," International Petroleum Technology Conference, Doha, Qatar, Nov., IPTC 10546.

[23] Kalyanraman, R. S., van Kujik, R., and Hori, H., 2017, "Making Sense of Why Sometimes Logs Do Not See Cement in the Annulus," SPE Western Regional Meeting, Bakersfield, CA, Apr. , SPE 185731.

[24] Jutten, J. J., and Hayman, A. J., 1993, "Microannulus Effect on Cementation Logs: Experiments and Case Histories," SPE Asia Pacific Oil and Gas Conference, Singapore, Feb., SPE 25377.

[25] Kalyanraman, R., Chen, X., Wu, P. Y., Constable, K., Govil, A., and Abubakar, A., 2021, "Autonomous Interpretation Methods of Ultrasonic Data Through Machine Learning Facilitates Novel and Reliable Casing Annulus Characterization," SPE/IADC Drilling Conference and Exhibition, Day 4 Thu, Mar. 11, 2021, SPE-204078.

[26] Viggen, E. M., Løvstakken, L., Måsøy, S.-E., and Merciu, I. A., 2021, "Better Automatic Interpretation of Cement Evaluation Logs Through Feature Engineering," SPE J., **26**(5), pp. 2894–2913.

[27] Viggen, E. M., Merciu, I. A., Løvstakken, L., and Måsøy, S.-E., 2020, "Automatic Interpretation of Cement Evaluation Logs From Cased Boreholes Using Supervised Deep Neural Networks," J. Petrol. Sci. Eng., **195**, p. 107539.

[28] Skadsem, H. J., Gardner, D., Beltrán-Jiménez, K., Govil, A., Palacio, G. O., and Delabroy, L., 2021, "Study of Ultrasonic Logs and Seepage Potential on Sandwich Sections Retrieved From a North Sea Production Well," SPE Drill. Complet., **36**(4), pp. 976–990.

[29] Beltrán-Jiménez, K., Gardner, D., Kragset, S., Gebremariam, K. F., Reales, O. M., Minde, M. W., de Souza, M. I. L., Aasen, J. A., Skadsem, H. J., and Delabroy, L., 2022, "Cement Properties Characterization From a Section Retrieved From an Oil Production Well After 33 Years of Downhole Exposure," J. Petrol. Sci. Eng., **208**, p. 109334.

[30] Brace, W. F., Walsh, J. B., and Frangos, W. T., 1968, "Permeability of Granite Under High Pressure," J. Geophys. Res., **73**(6), pp. 2225–2236.

[31] Hsieh, P. A., Tracy, J. V., Neuzil, C. E., Bredehoeft, J. D., and Silliman, S. E., 1981, "A Transient Laboratory Method for Determining the Hydraulic Properties of 'Tight' Rocks—I. Theory," Int. J. Rock Mech. Min. Sci. Geomech. Abstr., **18**(3), pp. 245–252.

[32] Dicker, A. I., and Smits, R. M., 1988, "A Practical Approach for Determining Permeability From Laboratory Pressure–Pulse Decay Measurements," SPE International Meeting on Petroleum Engineering, pp. 1–8, SPE 17578.

[33] Skadsem, H. J., 2021, "Fluid Migration Characterization of Full-Scale Annulus Cement Sections Using Pressure–Pulse-Decay Measurements," ASME J. Energy Resour. Technol., **144**(7), p. 073005.

[34] Moeinikia, F., Ford, E. P., Lohne, H. P., Arild, Ø., Majoumerd, M. M., and Fjelde, K. K., 2018, "Leakage Calculator for Plugged-and-Abandoned Wells," SPE Prod. Oper., **33**(4), pp. 790–801.

[35] Johnson, C., Sefat, M. H., and Davies, D., 2021, "Developing a Well-Centric Flow Model—The First Step in a Risk-Based Approach to Oil and Gas Well Decommissioning," J. Petrol. Sci. Eng., **204**, p. 108651.

[36] Hannon, Jr., M. J., 2016, "Alternative Approaches for Transient-Flow Laboratory-Scale Permeametry," Trans. Porous Med., **114**, pp. 719–746.

[37] Stehfest, H., 1970, "Algorithm 368: Numerical Inversion of Laplace Transforms," Commun. ACM, **13**(1), pp. 47–49.

[38] Yang, M., Neubauer, C., and Jennings, H., 1997, "Interparticle Potential and Sedimentation Behavior of Cement Suspensions: Review and Results From Paste," Adv. Cement. Based Mater., **5**(1), pp. 1–7.

[39] Stiles, D., and Baret, J., 1993, "Sedimentation and Free Water of Cement Slurries: Mathematical Models and Practical Solutions," SPE Rocky Mountain Petroleum Technology Conference/Low Permeability Reservoirs Symposium, SPE-25866-MS.